MIT Open Access Articles

Selective sulfidation of metal compounds

The MIT Faculty has made this article openly available. ***Please share*** how this access benefits you. Your story matters.

Citation: Stinn, Caspar and Allanore, Antoine. 2021. "Selective sulfidation of metal compounds." 602 (7895).

As Published: 10.1038/s41586-021-04321-5

Publisher: Springer Science and Business Media LLC

Persistent URL: https://hdl.handle.net/1721.1/153477

Version: Author's final manuscript: final author's manuscript post peer review, without publisher's formatting or copy editing

Terms of use: Creative Commons Attribution-Noncommercial-Share Alike

Selective Sulfidation of Metal Compounds

Caspar Stinn[1] and Antoine Allanore[1]*

[1.] Massachusetts Institute of Technology, Department of Materials Science and Engineering, Cambridge, MA, USA 02139-4307

*Corresponding author, allanore@mit.edu

There is urgent, unprecedented demand for critical, by- and coproduct metallic elements for the infrastructure (magnets, batteries, catalysts, electronics) needed to power society with renewable electricity[1–3]. However, extraction of these d- and f- block metals from mineral and recycled streams is thermodynamically difficult, typically requiring complete dissolution of the materials, followed by liquid-liquid separation using metal ion complexing or chelating behavior[4,5]. The similar electronic structure of these metals results in poor separation factors, necessitating immense energy, water and chemicals consumption[6–8]. Herein, a processing approach based on selective anion exchange is proposed. Several simple process levers (gas partial pressure, gas flowrate, carbon addition) were demonstrated to selectively sulfidize a target metal from a mixed metal oxide feed. The physical and chemical differences between the sulfide and oxide compounds (e.g. density, magnetic susceptibility, surface chemistry) can then be exploited for vastly improved separation over liquid-liquid methods[9]. The process conditions of sulfidation are provided for 56 elements and demonstrated for 15 of them. The assessment of the environmental and economic impacts suggests a path toward 60-90% reductions in greenhouse gas emissions while offering significant capital cost savings compared to liquid-liquid hydrometallurgy.

Main

Conventional separation of by- and coproduct materials consists of physical processing, followed by roasting, leaching, and liquid-liquid separation. Liquid-liquid pyrometallurgical separation methods, such as matte smelting for copper-iron separation, can exhibit lower energy inputs and environmental impacts than leaching and aqueous-organic liquid-liquid separation[10]. However, classical pyrometallurgy frequently lacks the selectivity necessary to separate critical by- and coproduct elements, such as cobalt from nickel or one rare-earth element from the others, thereby necessitating the subsequent use of more selective hydrometallurgical methods, with detrimental consequences to sustainability and cost. Achieving solid materials enrichment or separation prior to conventional liquid-liquid chemical separations is a promising way to reduce the environmental and economic impacts of this later stage. This can be accomplished by combining gas-solid anion exchange reactions and conventional solid-solid or solid-fluid physical separations prior to hydrometallurgical separation[11]. An anion exchange reaction selectively reacts a metal (M) from a compound mixture containing M-X to target the formation of a new compound M-Y. The compound M-Y is targeted to enable subsequent physical separation that was impractical with the original feedstock. Sulfidation, where Y is now sulfur (S), is a promising avenue to separate mixed oxides, where X is oxygen (O). Indeed, sulfidation is already employed industrially in catalyst production for S-C-O-H gas reactions[12,13]. Additionally, sulfide and oxide particles are effectively separated using physical methods; for example particles as small as 2.5 microns in size have been effectively separated at mining operations[14,15], while optimization of sulfidation operating conditions can lead to product phases on the order of tens of microns in size[16]. However, pyrometallurgical selective sulfidation is often dismissed industrially as unsuitable for scalable, continuous materials processing due to reliance on condensed or briquetted sulfur sources, found to hinder mass transfer and the overall rate of conversion of the process[17,18]. Kinetic and transport limitations to sulfidation conversion are not uncommon and may be overcome by using more powerful – yet toxic – sulfidizing agents such as H_2S[19] or CS_2[19,20] well-known in catalysis and mineral processing to facilitate *complete sulfidation* of mixed metal oxide compounds[21,22]. The feasibility of such approaches for mineral and recycling products is in doubt, in part due to the cost and challenges of such reactants as well as their lack of *selectivity*. Herein, we demonstrate a thermodynamic and kinetic framework to support selective sulfidation as an environmentally and economically sustainable process for critical by- and coproduct materials needed in modern technologies. We demonstrate the potential impact of selective sulfidation for lithium ion battery recycling, rare earth magnet recycling, and rare earth mineral processing, chosen as representative examples of metal processing applications required for a sustainable future, but presently hindered by technical challenges and high environmental impacts.

Sulfidation Thermodynamics and Kinetics

As illustrated in Figure 1a, the ease of separation of compounds is thermodynamically defined by the difference between their relative stabilities, described for oxides and sulfides by the oxygen and sulfur partial pressures necessary ($[P_{O2}]_{crit}$, $[P_{S2}]_{crit}$) for the reduction of a given metal compound. The partial pressures P_{O2} and P_{S2} during pyrometallurgical reduction are conventionally set by gas ratios such as CO/CO_2, H_2/H_2O, or H_2/H_2S, yet these ratios are difficult to control as those gases often react to form metal carbides or hydrides. Pyrometallurgical roasting controls sulfur, oxygen, and SO_2 partial pressures (P_{S2}, P_{O2}, and P_{SO2}) to stabilize oxides, sulfides, oxysulfides, or sulfates, as shown in the predominance (Kellogg) diagrams in Figure E1. By Le Chatelier's principle, a critical P_{S2}/P_{SO2} ratio, $[P_{S2}/P_{SO2}]_{crit}$, can be determined for a given sulfidation reaction to become thermodynamically spontaneous, presented in Figure

1a for 56 pure metal oxides and detailed in Table S1. The differences in $[P_{S2}/P_{SO2}]_{crit}$ between pure species and real materials can be accounted for by solution thermodynamics (Figure E2), as presented in Supplemental Materials. Unlike P_{O2} for oxide reduction alone, and P_{S2} for sulfide reduction alone, the P_{S2}/P_{SO2} ratio for sulfidation of an oxide can be precisely controlled, in principle supporting selective sulfidation of metal oxides. With the sulfide phases selectively formed within the solid material feed, physical separation based on physical property differences between oxide and sulfide phases becomes possible.

$[P_{S2}/P_{SO2}]_{crit}$, while defining the thermodynamic landscape of sulfidation, also delineates the permissible S_2 inlet and SO_2 accumulation for sulfidation to occur within a reactor, allowing for transport and kinetic effects to be considered. Three possibilities to control P_{S2} and P_{SO2} can be distinguished: i) the intrinsic rate of the sulfidation reaction, ii) the gas space time and velocity in and out of the reactor, and iii) the chemical reaction of S_2 and SO_2 with other species within the reactor. Carbon addition provides an additional leverage to increase the P_{S2}/P_{SO2} ratio during sulfidation, by chemically reducing SO_2 into elemental sulfur, establishing a *carbothermically-driven sulfur reflux* (CDSR) of SO_2. Combining these considerations (Supplemental Materials), critical gas flowrates for sulfidation may be determined as a function of carbon addition, reaction kinetics, and $[P_{S2}/P_{SO2}]_{crit}$, as illustrated in Figure 1b. An increase in the carbon to oxide feed ratio leads to a loss of selectivity due to co-sulfidation in the range of $[P_{S2}/P_{SO2}]_{crit}$ characteristic of many transition metals. This explains prior challenges with selectivity encountered in previous attempts to sulfidize mixed transition metal oxides such as Fe- Ni[23], Fe- Zn[24], and Fe-Cr[22]. Herein, we demonstrate carbon-free selective sulfidation of mixed transition metal oxides for lithium ion battery recycling.

Sulfidation is investigated in a well-characterized packed-bed reactor (Figure E3) using Sohn's criteria[25] for distinguishing mass transport limitations from intrinsic reaction kinetic effects (Supplemental Materials, Tables S2-S3). We measure activation energy and reaction order (Figure E4) for the sulfidation of La_2O_3 with S_2 above 1200°C, achieving >99% conversion of oxide to sulfide (Table S4). We then demonstrate sulfidation of pure scandium, zirconium, and tungsten oxides, as well as pure strontium and calcium carbonates, to their respective sulfides via reaction with S_2 using CDSR (Tables S5-S9). This shows the possibility of eliminating the use for CS_2 or H_2S as sulfidizing agents for materials needed in new microelectronic[26], magneto-optic[26], SO_2 capture[27], or novel electrolytic metallurgical processes dependent on high-purity alkaline, transition, and rare earth sulfide[28] feedstocks. For mixed oxides, we illustrate control of sulfidation selectivity through sulfidation reaction kinetics and carbon addition via CDSR. We demonstrate the possible leverage offered by thermal activation[29] differences to control the sulfidation of oxides with dissimilar melting temperatures. This is supported herein by kinetic control of sulfidation selectivity between iron and rare earth oxides (Fe_2O_3, Ln_2O_3, melting points 1597°C and ~2200-2500 °C) for the recycling of rare earth magnets. The control of sulfidation using CDSR is illustrated in Figure 1b, via manipulation of the carbon to oxide feed ratio, as demonstrated through the selective formation of oxysulfide and sulfide phases in the processing of synthetic rare earth minerals.

Lithium-Ion Battery Recycling

We demonstrate carbon-free selective sulfidation of nickel-manganese-cobalt oxide (NMC) cathode material for recycling of lithium ion batteries (LIBs) as a case study in selective sulfidation and separation of mixed metals with $[P_{S2}/P_{SO2}]_{crit}$ near unity, generally applicable for transition metal separations. With increasing adoption of electric vehicles, cobalt and lithium for

LIBs have faced periods of supply uncertainty characteristic of byproduct metals[30,31], motivating efforts to geographically diversify supply and lower emissions associated with their primary production[32]. Industrial pyrometallurgical processes for battery recycling lack selectivity for individual battery metals, requiring economically and environmentally-burdensome downstream leaching and subsequent hydrometallurgy to selectively recovery battery elements[2,6]. Meanwhile, direct hydrometallurgical and physical processes for LIB recycling face hurdles associate with convoluted chemistry streams and high costs[2,6,33]. However, cathode elements from end of life lithium ion batteries can be selectively sulfidized[34].

As reported in Figure 2a, upon sulfidation the LIB cathode melts and phase separates into three immiscible liquids: nickel-rich sulfide, cobalt-rich sulfide, and manganese oxysulfide. The clear macroscopic phase separation of nickel and cobalt from manganese (Figure E5) highlights the prospect of selective sulfidation for separation. Meanwhile elements that are difficult to separate from recycled streams, such as aluminum, are calcined as an oxide. When included in the sulfidation charge, with additional SO_2 fed into the reactor, aluminum remains as an oxide upon selective sulfidation (Supplemental). Crude flotation (Figure E3) of the crushed, sulfidized solid shows selective separation of nickel and cobalt from aluminum, lithium, and manganese at 82.8% purity, 52.8% recovery (Table S10). The distribution of lithium post sulfidation is unclear from microscopy (SEM-EDS), but is shown by QXRD (Table S11) to exist largely as water-soluble sulfate, and was leached prior to flotation at 83% recovery from all phases (Table S10). As a promising alternative to flotation, magnetic separation of cobalt and nickel from aluminum, manganese, and lithium was demonstrated at 82.1% product purity, 84.8% recovery (Table S10).

Our findings indicate that transition metal elements previously requiring a series of harsh pyrometallurgical and hydrometallurgical separations can now be isolated through a single, *pyrometallurgical sulfidation step to produce an intermediate feed amenable to simple, conventional physical separation technologies.*

Rare Earth Magnet Recycling

Leverage of sulfidation kinetics and solution thermodynamics is necessary for effective material separation from complex feeds via selective sulfidation. Rare earth element (Ln) extraction and separation from (Nd,Pr,Dy)-Fe-B magnets is chosen as a case study for kinetic control of sulfidation selectivity in real systems. Here we expect differences between the thermal activation of the sulfidation reaction for Fe and Ln oxides, and leverage the well-documented oxidation thermodynamics of Fe-Nd-B magnets[35]. The separation window for sulfidation expressed in $[P_{S2}/P_{SO2}]_{crit}$ for Fe_2O_3 and Ln_2O_3 (Figure 1a) is broadly reflective of many critical material separations, such as Sc extraction from red mud[36], recycling of Ln-transition metal catalysts[37], and Ln recovery from electrowinning slags[38].

Recycling of (Nd,Pr,Dy)-Fe-B magnets is a promising pathway to confront critical material supply uncertainty by redistributing the geography of Ln production, while a selective recovery facilitated by sulfidation could address the unbalanced supply and demand of different Ln, often termed the rare earth balance problem[39]. Many pyrometallurgical[40], hydrometallurgical[41], hydrogen[42], and liquid metal[43] processes have been explored for Ln recovery from (Nd,Pr,Dy)-Fe-B, whereas Ln-Ln separation typically follows the conventional hydrometallurgical separation pathway used in primary Ln production[37].

Following (Nd,Pr,Dy)-Fe-B demagnetization, crushing, Ni coating removal, and calcination (Methods), (Nd,Pr,Dy)-Fe-B magnet oxide was selectively sulfidized, forming FeS with $(Nd,Pr,B)_2O_3$ inclusions approximately 20-100 μm in size (Figure 2b). This size is promising to support comminution and physical separation of oxide and sulfide phases through optimization of nucleation, growth, and coarsening phenomena. Ln_2O_2S formation was thermodynamically predicted to accompany Fe_2O_3 sulfidation, yet was kinetically suppressed due to insufficient thermal activation. A combined Ln metals basis purity in the oxide regions of 99.7 mass% was achieved. Surprisingly, Dy was enriched in the FeS phase compared to the oxide region (Figure E6), even without the CDSR required for sulfidation of pure Ln_2O_3. The corresponding distribution ratio of Dy and Nd between the oxide inclusions and FeS phase, referred to as the separation factor in hydrometallurgy (Supplemental), was observed to be 711, a 100x improvement to Ln-Ln separation over emerging[44] or state of the art[8] hydrometallurgical processing. The unexpected, highly-effective partitioning of Dy apart from Nd/Pr is attributed to unknown solution thermodynamics of Ln-B-O-S systems, noting the role of B in accentuating Ln thermodynamic differences. This has been observed before for other, sulfur-free, Ln-Ln separations via borate crystalization[11]. Herein selective sulfidation for (Nd,Pr,Dy)-Fe-B magnet recycling, in addition to being a promising avenue for stabilizing and diversifying Ln supply, demonstrates the power of our novel, integrated, insights into solution thermodynamics and reaction kinetics for design of effective selective sulfidation separation systems.

Rare Earth Element Mineral Processing

For selective sulfidation of materials with high $[P_{S2}/P_{SO2}]_{crit}$, P_{S2}/P_{SO2} can be controlled through CDSR, as discussed here for separation of elements from mixed oxide phases. Among the most commercially-relevant sources of Ln remain fluorocarbonate (bastnaesite, $LnCO_3F$) and phosphate (monazite/xenotime, $LnPO_4$) minerals[45]. They currently call for unsustainable[7,9] acid or alkali roasting to decompose mixed-element and polyatomic anions, to manage normally-occurring radioactive materials (NORMs) such as thorium, and to form soluble compounds prior to solvent extraction for Ln separation[8]. More sustainable defluorination, dephosphorization, and dethoriation technologies have been proposed previously, but were less apt for subsequent liquid-liquid hydrometallurgy. They however provide conditions for the formation of Ln_2O_3 or Ln_2O_2S feed, suitable for selective sulfidation.

Upon heating, $LnCO_3F$ decomposes to LnOF and CO_2, with sulfidation of LnOF presently untenable for defluorination due to the formation of Ln oxyfluorosulfide (Table S12). However, defluorination of $LnCO_3F$ is readily conducted via roasting with Na_2CO_3, forming Ln_2O_3, CO_2, and water-soluble NaF that is easily removable via washing[8,46]. We herein observed dephosphorization of $LnPO_4$ via sulfidation with $CaCO_3$ to form Ln_2O_2S, SO_2, and calcium phosphate (Table S13) which is readily separated from Ln compounds via physical separation[8]. Merritt demonstrated that during monazite sulfidation in the presence of Na_2CO_3, thorium partitions to a separate oxide phase from Ln_2O_2S[47], consistent with our sulfidation series (Figure 1a), supporting dethoriation of Ln_2O_3 and $LnPO_4$ via sulfidation and physical separation. We also observed that sulfidation followed by calcination (sulfidative sintering) of finely-liberated (25-45 μm particle size) synthetic, defluorinated, dethoriated, bastnaesite results in sintered Ln_2O_3 particle sizes of up to 200 μm or more.

Following defluorination, dethoriation, and sulfidative-sintering, CDSR is leveraged for Ln separation via selective sulfidation of synthetic bastnaesite mixed with carbon at a mass feed ratio of Ln_2O_3 / C = 0.1 (Ln = La, Ce, Pr, Nd). Nd-rich Ln_2O_2S, La-rich $Ln_{10}OS_{14}$, and Ln_2S_3 product phases were observed through EPMA/WDS, demonstrating that selective enrichment of individual Ln from rare earth minerals is feasible via selective sulfidation (Figure 2c). Ln_2O_2S and $Ln_{10}OS_{14}$ phases were on the order of 20-100 μm in size (Figure E7), likely large enough for liberation and physical separation through process refinement, with Ln_2S_3 phases typically 10-20 μm in size and less-prevalent. A tradeoff exists between sulfidation selectivity, maximized at shorter solid residence times, and growth/coarsening of large phases that support liberation and physical separation, maximized at longer solid residence times. Optimization of sulfidation kinetics for Ln separation is presently hindered by unknown Ln_2O_2S/$Ln_{10}OS_{14}$/Ln_2S_3 reaction, nucleation, and growth phenomena, in addition to uncharted Ln_2O_2S/$Ln_{10}OS_{14}$ solution thermodynamics. Opportunities for increasing selectivity exist, for example with the addition of components that accentuate differences in Ln solution behavior, such as observed for boron in Ln separations from (Nd,Pr,Dy)-Fe-B magnets. *With further understanding of oxysulfide thermodynamics and structure, the results show that CDSR is a powerful tool for tuning sulfidation selectivity in systems with high* $[P_{S2}/P_{SO2}]_{crit}$*, such as for Ln separation.*

Technoeconomic Considerations

Selective sulfidation as investigated herein can be conducted at scale in conventional pyrometallurgical reactors for feed drying, roasting, and sulfidation. The product of sulfidation can be processed with conventional beneficiation technologies for comminution and physical separation of product phases. The capital structure of these processes is well-established[48], allowing for economic comparison of the capital costs (CAPEX) of selective sulfidation to presently-deployed hydrometallurgical technologies using scaling factor estimates (Supplemental Materials, Table S14). Comparison of operating cost (OPEX) meanwhile is hindered by unquantified variations depending on the location. Those include the actual materials feedstocks, the OPEX for hydrometallurgy at each location, and proprietary liquid-liquid extractor chemistry and liquid-liquid contactor employed[8].

The CAPEX of a generic, binary metal separation from equimolar mixed oxides is estimated for hydrometallurgical processing. Its flow-sheet consists of acid roasting for impurity removal and formation of soluble metal compounds, gas treatment, leaching of the target elements, solvent extraction for metal element separation, and precipitation of product metal compounds, with conditions reported in Table S15. Meanwhile, the CAPEX and OPEX for separation via selective sulfidation from the same mix is estimated by considering air separation for nitrogen carrier gas production, carbon-free sulfidation in a multihearth fluidized bed reactor, comminution, physical separation via froth flotation, and downstream gas handling and treatment (Figure E8), with conditions reported in Table S16-S17. The costs of some possible sulfidation feed preparation and impurity management techniques, such as feed drying, dehalogenation or dephosphorization via roasting/calcination, and sulfidation/calcination for sintering of material feeds are also considered, as well as costs surrounding the carbothermically-driven sulfur reflux (CDSR) (Figure S1-S3). Sensitivity analysis is conducted via Monte Carlo simulation as described in Methods and Supplemental Materials over conditions reported in Tables S15-S17, and is presented in Figures E9 and S4-S6.

For the generic binary separation of equimolar mixed metal oxides, the selective sulfidation pathway is predicted to offer a 65-90% reduction in CAPEX compared to hydrometallurgical separation at separation factors of 1.5-10,0000, representative of solvent extraction for f-block elements and d-block elements separation respectively[8] (Figure 3a). The OPEX of selective sulfidation is predicted to be on the order of \$50, \$100, and \$300 per tonne of feed at feed capacities of 1,000, 100, and 10 kilotonnes per year respectively (Table S18). Attribution of CAPEX and OPEX to individual processing steps are presented in Figures S5-S6. Pretreatment steps for feed drying, sintering, and roasting/calcination each marginally increase the CAPEX and OPEX of selective sulfidation by 10% to 20%. While preliminary CAPEX and OPEX estimates are promising, to understand the profitability of a given materials separation process utilizing selective sulfidation, detailed design considering geographic-specific factors (ore grade and impurities, labor costs and utilization, level of automation, greenfield versus established facility, CAPEX versus OPEX tradeoffs, etc.) and further refinement of sulfidation operating conditions and chemistries will be necessary. Regional and organizationally-specific factors pertaining to cost of capital, depreciation, and amortization are also critical for understanding the economic competitiveness of selective sulfidation.

Sustainability Considerations

Deploying selective sulfidation for f-block and d-block element separation means shifting from hydrometallurgy and chemical separations to pyrometallurgy and physical separations. To contextualize this shift, selective sulfidation / physical separation is compared via life cycle assessment (LCA) over equivalent system boundaries and functional units to industrial hydrometallurgy processes for alkali fusion / leaching of zirconium-silicon, dissolution / selective precipitation of iron-titanium, and acid roasting / solvent extraction of rare earth elements[9,49]. These processes are broadly representative of a range of hydrometallurgical technologies employed industrially, and all utilize a series of selective hydrometallurgical steps coupled with non-selective pyrometallurgical roasting. For a generic sulfidation process without CDSR (as described in Technoeconomic Consideration, Figure E8), the global warming potential (GWP), terrestrial acidification (TA), and water resource depletion (WRD) are estimated to be on the order of 0.20 (+/- 0.06) kg CO_2-eq, $9x10^{-3}$ (+/- $5x10^{-3}$) kg of SO_2-eq, and 9 (+/- 4) kg H_2O respectively per kg of feed, presented in Figure E10. The inclusion of pretreatments such as feed drying, calcination/roasting, and sintering (Figure S2) on average increase GWP by about 50%, WRD by 30% and TA by double over the base case (Table S18). The use of CDSR in selective sulfidation (Figures S1, S3) meanwhile increases GWP by a factor of 4-5x and WRD by a factor of 3-4x. This suggests that CDSR is best reserved for use in materials separation challenges plagued by particularly high environmental impacts, such as rare earth element production. Sensitivity analysis is conducted through Monte Carlo simulation over conditions reported in Tables S16-S17, detailed in Methods and Supplemental Materials. The sustainability of every materials separation challenge is influenced differently by feedstock chemistry, grade, and purity, and deserves its own detailed analysis beyond the generic sulfidation pathway proposed in Technoeconomic Considerations.

For the environmental case studies of zirconium-silicon, iron-titanium, and rare earth element separation, process flowsheets and system boundaries for selective sulfidation are included in Figures S7-S10. The operating conditions are found in Tables S19-S21 and their detailed life cycle inventories in Tables S22-S24. Processing steps, assumptions, and allocation strategies (Table S25) are discussed in Methods and Supplemental Materials. Selective sulfidation with physical separation is predicted to reduce the GWP by over 80% when compared to both the hydrometallurgical zirconium-silicon and titanium-iron separations[49] (Figure 3b, Table S26). Meanwhile, selective sulfidation with CDSR and physical separation for rare earth separation is predicted to reduce GWP by 60-90%, TA by 70%, and WRD by 65-85% versus conventional[9] hydrometallurgical processing of bastnaesite via acid roasting, leaching, and solvent extraction (Figure 3b, Tables S26-S27). Uncertainty exists due to a lack of primary process operational data, proprietary in the case of published hydrometallurgy studies, and undemonstrated at commercial scale in the case of selective sulfidation. The anticipated environmental improvements compared to water and energy-intensive hydrometallurgy are not surprising however, as sulfidation requires limited energy inputs due to the exothermic nature of sulfidation reactions (Tables S28-S30) and effective sulfur dioxide emissions abatement methods. Meanwhile, comminution and physical separations are expected to be less energy-intensive than leaching for separation of products with the grain sizes obtained via selective sulfidation[50]. *Our results indicate that when pyrometallurgical methods are sufficiently selective to minimize the need for subsequent hydrometallurgical treatments, as demonstrated experimentally herein using selective sulfidation, the environmental impact of materials processing may be lowered.*

Conclusions

Processing of critical d and f-block elements for high-tech and green technologies presently requires expensive and unsustainable hydrometallurgical separations, yet sulfur chemistry can support alternative separation methods with environmental benefits and cost competitiveness. We show for the first time that through an integrated view of thermodynamics and kinetics, selective sulfidation is applicable for difficult rare earth and transition metal separations, such as required for rare earth magnet and lithium ion battery recycling. While sulfidation and subsequent physical separation processes require optimization, the framework established herein charts a new path forward for reducing the water demand, energy usage, emissions, and materials costs of an electrified, sustainable future.

Main References

1. Cheisson, T. & Schelter, E. J. Rare earth elements: Mendeleev's bane, modern marvels. *Science (80-.).* **363**, 489–493 (2019).
2. Harper, G. *et al.* Recycling lithium-ion batteries from electric vehicles. *Nature* **575**, 75–86 (2019).
3. Enriquez, M. A. *et al.* Mineral supply for sustainable development requires resource governance. *Nature* **543**, 367–372 (2017).
4. Reck, B. K. & Graedel, T. E. Challenges in Metal Recycling. *Science (80-.).* **337**, 690–696 (2012).

5. Olivetti, E. A. & Cullen, J. M. Toward a sustainable materials system. *Science (80-.).* **360**, 1396–1398 (2018).

6. Ciez, R. E. & Whitacre, J. F. Examining different recycling processes for lithium-ion batteries. *Nat. Sustain.* **2**, 148–156 (2019).

7. K Lee, J. C. & Wen, Z. Pathways for greening the supply of rare earth elements in China. *Nat. Sustain.* **1**, 598–605 (2018).

8. Zhao, B., Zhang, J. & Schreiner, B. *Separation Hydrometallurgy of Rare Earth Elements*. (Springer International Publishing AG Switzerland, 2016).

9. Bailey, G. *et al.* Review and new life cycle assessment for rare earth production from bastnäsite, ion adsorption clays and lateritic monazite. *Resour. Conserv. Recycl.* **155**, 104675 (2020).

10. Norgate, T. & Jahanshahi, S. Low grade ores – Smelt, leach or concentrate? *Miner. Eng.* **23**, 65–73 (2010).

11. Yin, X. *et al.* Rare earth separations by selective borate crystallization. *Nat. Commun.* **8**, (2017).

12. Flytzani-Stephanopoulos, M., Sakbodin, M. & Wang, Z. Regenerative Adsorption and Removal of H2S from Hot Fuel Gas Streams by Rare Earth Oxides. *Science (80-.).* **312**, 1508–1510 (2006).

13. Valsamakis, I. & Flytzani-Stephanopoulos, M. Sulfur-tolerant lanthanide oxysulfide catalysts for the high-temperature water-gas shift reaction. *Appl. Catal. B Environ.* **106**, 255–263 (2011).

14. Pease, J. D., Curry, D. C. & Young, M. F. Designing flotation circuits for high fines recovery. *Miner. Eng.* **19**, 831–840 (2006).

15. Pease, J. D., Young, M. F., Curry, D. & Johnson, N. W. Improving fines recovery by grinding finer. *Trans. Institutions Min. Metall. Sect. C Miner. Process. Extr. Metall.* **119**, 216–222 (2010).

16. Han, J. *et al.* Effects of sodium salts on the sulfidation of lead smelting slag. *Miner. Eng.* **108**, 1–11 (2017).

17. Zhang, W., Zhou, Y., Zhu, J. & Pan, Y. New clean process for barium sulfide preparation by barite reduction with elemental sulfur. *Ind. Eng. Chem. Res.* **53**, 5646–5651 (2014).

18. Zhang, W. *et al.* Reaction mechanism study of new scheme using elemental sulfur for conversion of barite to barium sulfide. *Powder Technol.* **360**, 1348–1354 (2020).

19. Kaneko, T., Yashima, Y., Ahmadi, E., Natsui, S. & Suzuki, R. O. Synthesis of Sc sulfides by CS2 sulfurization. *J. Solid State Chem.* **285**, 121268 (2020).

20. Ahmadi, E. & Suzuki, R. O. An Innovative Process for Production of Ti Metal Powder via TiS x from TiN. *Metall. Mater. Trans. B* **51B**, 140–148 (2020).

21. Afanasiev, P. *et al.* Preparation of the mixed sulfide Nb2Mo3S10 catalyst from the mixed oxide precursor. *Catal. Letters* **64**, 59–63 (2000).

22. Ahmad, S., Rhamdhani, M. A., Pownceby, M. I. & Bruckard, W. J. Thermodynamic assessment and experimental study of sulphidation of ilmenite and chromite. *Trans. Institutions Min. Metall. Sect. C Miner. Process. Extr. Metall.* **123**, 165–177 (2014).

23. Harris, C. T., Peacey, J. G. & Pickles, C. A. Selective sulphidation and flotation of nickel from a nickeliferous laterite ore. *Miner. Eng.* **54**, 21–31 (2013).

24. Liu, W., Zhu, L., Han, J., Jiao, F. & Qin, W. Sulfidation mechanism of ZnO roasted with pyrite. *Sci. Rep.* **8**, 9516 (2018).

25. Sohn, H. Y. & Fan, D.-Q. On the Initial Rate of Fluid-Solid Reactions. *Met. Mater. Trans.*

B **48B**, 1827–1832 (2017).

26. Zagorac, D., Doll, K., Zagorac, J., Jordanov, D. & Matovic, B. Barium Sulfide under Pressure: Discovery of Metastable Polymorphs and Investigation of Electronic Properties on ab Initio Level. *Inorg. Chem.* **56**, 10644–10654 (2017).
27. Sohn, H. Y. & Kim, B.-S. A Novel Cyclic Process using CaSO 4 /CaS Pellets for Converting Sulfur Dioxide to Elemental Sulfur without Generating Secondary Pollutants: Part I. Feasibility and Kinetics of the Reduction of Sulfur Dioxide with Calcium-Sulfide Pellets. *Metall. Mater. Trans. B* **33B**, 711–716 (2002).
28. Sahu, S. K., Chmielowiec, B. & Allanore, A. Electrolytic Extraction of Copper, Molybdenum and Rhenium from Molten Sulfide Electrolyte. *Electrochim. Acta* **243**, 382–389 (2017).
29. Brown, A. M. & Ashby, M. F. Correlations for diffusion constants. *Acta Metall.* **28**, 1085–1101 (1980).
30. Nassar, N. T., Graedel, T. E. & Harper, E. M. By-product metals are technologically essential but have problematic supply. *Sci. Adv.* **1**, e1400180 (2015).
31. Olivetti, E. A., Ceder, G., Gaustad, G. G. & Fu, X. Lithium-Ion Battery Supply Chain Considerations: Analysis of Potential Bottlenecks in Critical Metals. *Joule* **1**, 229–243 (2017).
32. Dunn, J. B., Gaines, L., Sullivan, J. & Wang, M. Q. Impact of Recycling on Cradle-to-Gate Energy Consumption and Greenhouse Gas Emissions of Automotive Lithium-Ion Batteries. *Environ. Sci. Technol.* **46**, 12704–12710 (2012).
33. Shi, J. *et al.* Sulfation Roasting Mechanism for Spent Lithium-Ion Battery Metal Oxides Under SO2-O2-Ar Atmosphere. *JOM* **71**, 4473–4481 (2019).

34. Stinn, C. & Allanore, A. Selective Sulfidation and Electrowinning of Nickel and Cobalt for Lithium Ion Battery Recycling. in *Ni-Co 2021: The 5th International Symposium on Nickel and Cobalt* (eds. Anderson, C. et al.) 99–110 (Springer Nature Switzerland AG, 2021). doi:10.1007/978-3-030-65647-8_7

35. Wagner, M.-E. & Allanore, A. Chemical Thermodynamic Insights on Rare-Earth Magnet Sludge Recycling. *ISIJ Int.* **60**, 2339–2349 (2020).

36. Narayanan, R. P., Kazantzis, N. K. & Emmert, M. H. Selective Process Steps for the Recovery of Scandium from Jamaican Bauxite Residue (Red Mud). *ACS Sustain. Chem. Eng.* **6**, 1478–1488 (2018).

37. Jowitt, Si. M., Werner, T. T., Weng, Z. & Mudd, G. M. Recycling of the Rare Earth Elements. *Curr. Opin. Green Sustain. Chem.* **13**, 1–7 (2018).

38. Wang, J. & Hu, H. Selective extraction of rare earths and lithium from rare earth fluoride molten-salt electrolytic slag by sulfation. *Miner. Eng.* **160**, 106711 (2021).

39. Binnemans, K., Jones, P. T., Müller, T. & Yurramendi, L. Rare Earths and the Balance Problem: How to Deal with Changing Markets? *Journal of Sustainable Metallurgy* **4**, 126–146 (2018).

40. Firdaus, M., Rhamdhani, M. A., Durandet, Y., Rankin, W. J. & McGregor, K. Review of High-Temperature Recovery of Rare Earth (Nd/Dy) from Magnet Waste. *J. Sustain. Metall.* **2**, 276–295 (2016).

41. Lin, X. *et al.* A novel application of hematite precipitation for high effective separation of Fe from Nd-Fe-B scrap. *Sci. Rep.* **9**, 1–8 (2019).

42. Jönsson, C. *et al.* The extraction of NdFeB magnets from automotive scrap rotors using hydrogen. *J. Clean. Prod.* **277**, 124058 (2020).

43. Rasheed, M. Z. *et al.* Review of the Liquid Metal Extraction Process for the Recovery of Nd and Dy from Permanent Magnets. *Metall. Mater. Trans. B* **52**, 1213–1227 (2021).

44. Li, X. Z. *et al.* A supramolecular lanthanide separation approach based on multivalent cooperative enhancement of metal ion selectivity. *Nat. Commun.* **9**, 547 (2018).

45. Jordens, A., Cheng, Y. P. & Waters, K. E. A review of the beneficiation of rare earth element bearing minerals. *Miner. Eng.* **41**, 97–114 (2013).

46. Chi, R., Li, Z., Peng, C., Gao, H. & Xu, Z. Preparation of enriched cerium oxide from bastnasite with hydrochloric acid by two-step leaching. *Metall. Mater. Trans. B Process Metall. Mater. Process. Sci.* **37**, 155–160 (2006).

47. Merritt, R. R. High Temperature Methods for Processing Monazite: II. Reaction with Sodium Carbonate. *J. Less-Common Met.* **166**, 211–219 (1990).

48. Woods, D. R. Appendix D: Capital Cost Guidelines. in *Rules of Thumb in Engineering Practice* 376–436 (Wiley-VCH Verlag GmbH & Co. KGaA, 2007). doi:10.1002/9783527611119.app4

49. Nuss, P. & Eckelman, M. J. Life cycle assessment of metals: a scientific synthesis. *PLoS One* **9**, e101298 (2014).

50. Skinner, B. J. Earth resources (minerals/metals/ores/geochemistry/mining). *Proc. Natl. Acad. Sci. USA* **76**, 4212–4217 (1979).

Main Figures

Figure 1: Sulfur to sulfur dioxide ratio for selective sulfidation of metals, and the corresponding gaseous space time, space velocity, and carbothermically-driven sulfur reflux (CDSR) levers. a – Oxide-sulfide anion exchange chemistry exacerbates the thermodynamic differences between metal compounds, illustrated at 1000°C in the relative

spacing and order of elements across the span of P_{S2}/P_{SO2} dioxide ratios required for oxide sulfidation (y-axis $[P_{S2}/P_{SO2}]_{crit}$) and the sulfur or oxygen partial pressures for oxide or sulfide reduction to metal (color for $[P_{S2}]_{crit}$ and x-axis for $[P_{O2}]_{crit}$), as described by the reactions tabulated in Table S1. **b** – $[P_{S2}/P_{SO2}]_{crit}$ is set in a sulfidation reactor for a maximum gas space time (τ^{max}_{space}, left) or minimum space velocity (v^{min}_{space}, right) through control of the carbon to metal oxide molar feed ratio (C/M_2O_3) via CDSR, tabulated here for a well-mixed gas phase at 1000°C and M_2O_3 at 60% of its melting temperature (homologous temperature, T_H) using La_2O_3 sulfidation kinetics observed for the same T_H. Excess carbon addition results in selectivity challenges for the $[P_{S2}/P_{SO2}]_{crit}$ characteristic of many transition metals ($\sim10^{-5}$ to $\sim10^{-1}$) due to co-sulfidation at a given τ^{max}_{space} and v^{min}_{space}.

Figure 2: Application of selective sulfidation for lithium ion battery recycling (a), rare earth magnet recycling (b), and rare earth mineral processing (c). a – $LiNi_{1/3}Mn_{1/3}Co_{1/3}O_2$ (abbr. NMC111 or NMC333) sulfidized for one hour at 1000°C which separates into Ni-rich sulfide (1, $Ni_{0.75}Co_{0.25}S$), Co-rich sulfide (2, $Ni_{0.33}Co_{0.67}S$), and Mn oxysulfide (3, $MnO_{0.2}S_{0.8}$) phases as identified with SEM/EDX of approximately 100-200 µm in size (SEM/BEC image). **b** – Rare earth, iron, boron ((Nd,Pr,Dy)-Fe-B) magnet demagnetized at 500°C, ground to 90-212 µm, calcined at 1000°C, and sulfidized for one hour at 1200°C separates into neodymium-rich regions (1, $Nd_{18.70}Pr_{4.26}Dy_{<0.01}Fe_{0.16}B_{10.35}O_{66.47}S_{0.06}$) precipitated out from the iron-rich (2, $Nd_{0.13}Pr_{0.02}Dy_{0.04}Fe_{45.55}B_{<0.01}O_{1.29}S_{52.96}$) sulfide phases as identified with WDS/EPMA of approximately 20-100 µm in size (SEM/BEC image). This corresponds to separation factors for Nd/Fe of 40500, Pr/Fe of 51400, Nd/Dy of 712, and Pr/Dy of 903 between the oxide (1) and sulfide (2) phases. **c** – Synthetic 25-45 µm, defluorinated, dethoriated, light rare earth element (Ln) bastnaesite ($(Ce,La,Pr,Nd)_2O_3$) sulfidatively sintered to 100-300 µm, then sulfidized with

carbon (C / Ln_2O_3 mass ratio = 0.12) four one hour at 1400°C, which separates into $Ln_{10}OS_{14}$ (1) and neodymium-enriched, La-depleted Ln_2O_2S (2, Nd 1.6x enriched from bulk, La 0.7x depleted from bulk) phases of approximately 20-100 μm in size as identified with WDS/EPMA, with less-prevalent Ln_2S_3 phases 10-20 μm in size (polarized optical image, 90°).

Figure 3: Capital costs and environmental impact estimates for selective sulfidation coupled with physical separation, compared with conventional hydrometallurgical processing. a – Selective sulfidation with physical separation is predicted to exhibit lower total fixed capital costs for binary metal oxide (M_A, M_B) separations than conventional mixer-settler or pulsed column liquid-liquid hydrometallurgy with acid roasting and leaching pretreatments, for both transition metals (hydrometallurgical separation factor $\beta = 10{,}000$) and rare earth metals ($\beta = 1.5$). Error bars correspond to +/- one standard deviation, as determined through Monte Carlo analysis. **b. –** Selective sulfidation (symbol: o) with physical separation is predicted to show significantly lower global warming potential than conventional hydrometallurgical technologies (symbol: ◇) such as alkali fusion with leaching (Zr-Si separation), leaching with selective precipitation (Ti-Fe separation), and acid roasting with leaching and solvent extraction (rare earth element separation). Data for hydrometallurgical technologies are adopted from published studies[9,49]. Error bars determined through Monte Carlo analysis correspond to +/- 2 standard deviations. System boundaries, operating conditions, life cycle inventories, and allocation methods are included in Figures S7-S10 and Tables S22-S24.

Methods

Sulfidation Precursors

For sulfidation experiments, elemental sulfur (99.5%, sublimed, Acros Organics) was utilized as the sulfidizing agent, with argon (99.95%, UHP300, Airgas) as a carrier gas. For sulfidation reactions where elevated levels of SO_2 were required, sulfur was combusted with oxygen (O_2, UHP300, Airgas) and used as a carrier gas in conjunction with argon. For sulfidation reaction kinetics studies, lanthanum(III) oxide (La_2O_3, 99.99% trace metal basis, Acros Organics) was utilized as the oxide precursor. The particle size distribution was determined via laser diffraction (Beckman Coulter Inc., LS 13320) of oxide samples suspended in water. The Brunauer–Emmett–Teller (BET) specific surface area was measured via N_2 gas absorption (Micromeritics ASAP 2020 surface area and porosity analyzer).

For demonstration of sulfidation of other pure oxides and carbonates, scandium(III) oxide (Sc_2O_3), zirconium(IV) oxide (ZrO_2, 99.5% metals basis, 1 μm APS, Alfa Aesar), tungsten(VI) oxide (WO_3, <100nm, Aldrich), calcium carbonate ($CaCO_3$, 99.0% purity, Alfa Aesar), and strontium carbonate ($SrCO_3$, 99% Sr, 1% Ba, -325 mesh, Alfa Aesar) were utilized as precursors. Target particle sizes for sulfidation precursors, when not specified by the supplier, were achieved by grinding oxide and carbon precursors using a mortar and pestle, and separated by particle size via sieving with stacking mesh trays.

For nickel-manganese-cobalt oxide (NMC) battery cathode recycling, simulated NMC cathode ($LiNi_{1/3}Mn_{1/3}Co_{1/3}O_2$, 98% purity, <0.5 μm, Aldrich) and alumina (Al_2O_3, 99.95% metals basis, 0.25-0.45 μm APS powder, Alpha Aesar) were utilized as oxide precursors.

For rare earth magnet recycling, nickel-plated iron-neodymium-praseodymium-dysprosium-boron magnet cubes (Ni-plated Fe-Nd-Pr-Dy-B, Grade 45, 6.25mm, McMaster-Carr) were demagnetized by heating under air at 500°C for two hours, then crushed to 90-212 μm in size. During crushing, the nickel coating deformed instead of shattered and was readily separated from Fe-Nd-Pr-Dy-B during sieving. Following crushing and sieving, Fe-Nd-Pr-Dy-B was calcined under air at 1000°C for 5 hours in a boron nitride crucible (20 mm OD, 14 mm ID, 32 mm depth, 3 mm bottom thickness) fabricated in-house from machinable boron nitride rod stock (BN, Saint-Gobain). Following calcination, the Fe-Nd-Pr-Dy-B-oxide was reground to 90-212 µm in size, forming the sulfidation precursor.

For rare earth mineral processing, monazite was simulated using lanthanum phosphate hydrate ($LaPO_4*xH_2O$, Alfa Aesar) dehydrated by heating to 1200°C over the course of 3 hours. Bastnaesite was simulated using lanthanum oxyfluoride synthesized from lanthanum(III) oxide (La_2O_3, 99.99% trace metal basis, Acros Organics) mixed stoichiometrically with lanthanum fluoride (LaF_3 anhydrous, 99.9% rare earth oxide basis, Alfa Aesar), then held at 1427°C for 28 hours in a graphite crucible under argon. For dephosphorization and defluorination, calcium carbonate ($CaCO_3$, ACS 99.0%, Alfa Aesar) was employed. Dethoriated, defluorinated bastnaesite was simulated by mixing cerium(IV) oxide (CeO_2, 99.9% metals basis, Aldrich Chemistry), lanthanum(III) oxide (La_2O_3, 99.99% trace metal basis, Acros Organics), neodymium oxide (neodymium(III) oxide (Nd_2O_3, 99.9%-Nd REO basis, Strem Chemicals), and praseodymium (III,IV) oxide (Pr_6O_{11}, 99.9%-Pr REO basis, Strem Chemicals) in ratio to match the metal content of natural bastnaesite from Mountain Pass, California, USA[45]. The mixed rare earth oxide was pressed into a rod (1.2 cm diameter, 8 cm long), sintered under air at 1580°C for 10 hours, then melted under argon in a floating zone optical furnace. Solidified mixed rare earth oxide was then ground to 25-45 µm in size, forming the synthetic dethoriated, defluorinated bastnaesite sulfidation precursor. To sulfidatively sinter the 25-45 µm synthetic dethoriated, defluorinated bastnaesite, the powder was sulfidized at 1450°C in a carbon crucible (see below) using sulfur gas at a partial pressure of 0.05-0.2 atm in argon carrier gas. The resulting sulfidized chunk was ground to 90-212 µm in size, then calcined under air at 1000°C for 5 hours in an alumina weigh boat. For selective sulfidation, graphite (C, 99.995%, Alfa Aesar) ground to 90-212 μm in size was utilized as the carbon source.

Sulfidation Reactor

Sulfidation experiments were performed in either a graphite or alumina packed-bed reactor, held within an alumina tube (600 mm length, 25mm OD, 21 mm ID) in a vertical tube furnace (Figure E3). For pure species sulfidation experiments, a graphite reactor was utilized, which was machined in-house from EDM graphite (Isostatically Pressed, EC-12 / AC-12, Tokai Carbon**)** in two parts – a graphite outer crucible (20 mm OD, 18 mm ID, 35 mm depth, 3mm bottom thickness) with holes (0.8 mm diameter, spaced 2 mm apart radially and laterally from center out to edge) in the bottom to allow for gas flow into the reactor. Placed at the bottom of the crucible was a shorter graphite crucible oriented upside down (17.5 mm OD, 13 mm ID, 3 mm depth, 3 mm bottom thickness) with holes offset from the outer crucible (0.8 mm diameter, spaced 2mm apart radially and laterally from center out to edge) to minimize oxide powder loss and to provide additional carbon to the system. For selective sulfidation experiments, an alumina reactor was utilized, which was machined in house from machinable alumina (96% Al_2O_3, Rescor 960, Cotronics Corp) as a single crucible (20 mm OD, 14 mm ID, 32 mm depth, 3 mm bottom thickness, with holes (1 mm diameter, spaced 2 mm apart radially and laterally from center out to edge) in the bottom for gas flow into the reactor. Sulfidation precursor powder was added to the packed bed reactor with bed porosities of 80-90% to minimize internal mass transfer effects within the packed bed of the reactor. Minor sintering and contraction of the sulfidation precursor powder into a pellet was observed during sulfidation, resulting in a wall gap on the order of 1mm between the crucible wall and the pellet during sulfidation, providing an unobstructed gas flow path through the holes in the bottom of the crucible and around the pellet.

The packed bed reactor was positioned in the hotzone of the furnace and supported on an alumina tube (300 mm length, 20 mm OD, 16 mm ID). Inside the alumina support tube was a stainless-steel 316 crucible (13 mm OD, 12 mm ID, depth 75 mm, bottom thickness 5 mm) containing elemental sulfur. The sulfur in the stainless-steel crucible was melted prior to sulfidation experiments outside of the furnace using a heat gun. Throughout the course of sulfidation, the crucible containing sulfur was moved up towards the hotzone of the furnace stepwise at a rate of either 2.5 mm / 2.5 minutes minute in the case of sulfidation kinetics experiments or 5 mm / 5 minutes for other sulfidation experiments via the raising of a mullite support rod (6 mm diameter). The movement of the sulfur-containing crucible toward the furnace hotzone allowed for the sulfur in the crucible to slowly melt then subsequently evaporate, supplying a sulfur gas flow through the furnace at a partial pressure of 0.05-0.2 atm. Care was taken in selection of the inner diameter of the reactor alumina support tube and the outer diameter of the stainless-steel sulfur crucible to avoid the crucible becoming pinned within the alumina support tube as the crucible was raised due to differences in thermal expansion. An argon carrier gas was flowed through the reactor at a flowrate of 1000 sccm to aid in sulfur gas transport and to minimize mass transfer limitations external to the packed bed within the reactor. For experiments where oxygen was used as a carrier gas in conjunction to argon, the mullite support rod also served as the oxygen inlet, facilitating combustion of sulfur with oxygen to meet required levels of sulfur dioxide within the reactor. Unless otherwise stated, sulfidation was conducted for 1 hour at the reaction conditions. Reaction conditions are discussed in the main text and included in Tables S4-S13.

Gas Handling and Analysis

For analysis of sulfidation product gasses, an IR / electrochemical gas analyzer (IR208, Infrared Industries) was utilized to measure the composition of hydrogen sulfide (H_2S), sulfur dioxide (SO_2), carbon monoxide (CO), carbon dioxide (CO_2), and oxygen (O_2) in the product gas stream. Before entering the gas analyzer, the gas stream traveled through a gravity separator and particle filters to clean the gas line of finely condensed unreacted sulfur particles that would clog the gas analyzer. After filtration of condensed sulfur particles, the gas stream was diluted with additional argon carrier gas to ensure that CO or SO_2 concentrations would not exceed the 1% upper limit of the gas analyzer. Following analysis, the product gas was then passed through a sodium hydroxide scrubber to remove and neutralize any H_2S or SO_2 in the product gas line.

Even when no sulfidation reaction was taking place, H_2S was observed in small flowrates (0.1-0.5 sccm) proportional to the sulfur evaporation rate and dilution. The H_2S signal was reproducible at a given rate of sulfur introduction independent of whether oxide or sulfide was present in the reactor. The sulfur flowrate through the course of the sulfidation reaction was therefore determined by integrating the H_2S flowrate and comparing that flowrate to the total mass of evaporated sulfur as measured by mass loss in the stainless-steel crucible holding the sulfur. Comparison to the total gas flow in the reactor allowed for calculation of the sulfur partial pressure in the reactor and the partial pressure ratios of sulfur to sulfur dioxide. Integration and mass balance over the CO, CO_2, and SO_2, signals allowed for determination of the conversion of oxygen liberated from the oxide starting material as a result of sulfidation.

Sulfidized Product Flotation, Leaching, and Magnetic Separation

For flotation studies of selectively sulfidized samples, a Hallimond-style flotation cell was constructed from quartz tubing (25 mm OD, 23 mm ID) and stainless-steel fittings fabricated in-house (Figure E3). Compressed air at a flowrate of 100 sccm was bubbled into the column through a stainless steel 316 frit (20 mm diameter, 1.5 mm thickness, 2 μm pore size, McMaster-Carr) epoxied around the inside the gas inlet fitting and in the center 8 mm of the frit, providing a region for tailings to settle. The resultant bubbles were on the order of 0.5 to 1 mm in diameter. The inlet gas fitting with frit was connected directly to a quartz column (25 mm OD, 23 mm ID, 1.2 m height). At the top of the column was another stainless-steel fitting machined in-house that formed a 45° connection to another quartz tube serving as a gas outlet and a T-fitting that connected the column and gas outlet to the concentrate collector, a closed-ended quartz tube. For flotation, potassium amyl xanthate (KAX) ($C_6H_{11}KOS_2$, >97% purity, Tokyo Chemical Industry) at a concentration of $5x10^{-3}$ M in deionized water was employed as the collector. No additional frothers or modifiers were utilized, however the KAX showed some frothing character. Flotation samples were on the order of 1 – 2 grams, and conditioned in 100 mL of the KAX solution. Upon initiating flotation, the column was filled a quarter of the way with the KAX solution, the conditioned sample and supporting KAX solution were added, then the column was rapidly, yet gently, filled with the remaining KAX so that the liquid level fully filled the collector chamber and connected the collector chamber to the column, resulting in a total KAX solution volume in the flotation cell of 750 mL. The flow of bubbles was then started and flotation of the sample conducted. Conditioning and flotation conditions are summarized with flotation results in Table S10. The flotation apparatus was tested in separation of copper sulfide (Cu_2S, 99.5% pure metal basis, Alfa Aesar) from iron oxide (Fe_2O_3, 99.5% pure metal basis, Alfa Aesar). Post flotation, the resulting concentrate and tailings were collected, dried, and analyzed for composition via ICP-OES.

Prior to NMC cathode flotation, leaching was performed to remove soluble Li_2SO_4 sulfidation products that were observed to suppress the flotation of Ni-Co sulfides by KAX. The sulfidized

NMC cathode was ground to a particle size of 149-212 μm, then stirred in de-ionized water at 10 g/L, neutral pH, and 20°C for 15 minutes to leach soluble lithium. The insoluble cathode materials were subsequently dried under vacuum at 200°C for 1 hour prior to flotation.

Magnetic separation of NMC cathodes sulfidized at 1000°C under a P_{S2}/P_{SO2} ratio of 3, ground to a particle size of 212-149 μm, was conducted by passing a flat, rare earth magnet disk (75 mm diameter, 3 mm thickness) directly over the ground cathode material. When sulfidized at P_{S2}/P_{SO2} ratios higher than 3, the cathode material did not respond to the magnet.

Sulfide Product Analysis

Sulfide products were analyzed for oxide to sulfide conversion via mass change and gas signal integration (Supplemental). Additionally, for lanthanum sulfide products, LECO combustion with oxygen was employed to determine sulfur content by quantification of SO_2 in the combustion product gasses using non-dispersive infrared (NDIR) sensors. For the oxygen content of lanthanum sulfide products, LECO gas fusion analysis was performed by heating the sample in a graphite crucible until the oxygen of the sample fully reacted with the carbon of the crucible, with oxygen content determined by quantification of the product CO and CO_2 gasses using NDIR sensors.

Sulfide product phase analysis was conducted on samples, crushed and ground with a mortar and pestle, via QXRD (Panalytical X'Pert MPD diffractometer), scanned over a range of 6°to 80° with a step size of 0.0131°, count time of 250 seconds per step, using Cu radiation at 45KV/40mA. Phases were identified using powdered diffraction files published by the International Centre for Diffraction Data or the Inorganic Crystal Structure Database.

Amorphous content was quantified by mixing a known amount of reference material (Al_2O_3 or ZnO) with the sample, re-running the scan under the same conditions as without the reference, and comparing the two XRD patterns adjusted for differences in scattering power. The difference between the integrated density of the peaks from the reference material and the observed crystalline phases as a fraction of the total corresponded to the amorphous content of the sulfidized product.

Localized microstructure and sulfidation product composition were analyzed via scanning electron microscopy (SEM, JEOL JSM-6610LV, JEOL Ltd.) utilizing energy dispersion spectroscopy analysis (EDS, Sirius SD detector, SGX Sensortech Ltd.). Electron probe microanalysis and wavelength dispersive X-ray analysis (EPMA, WDS, JEOL-JXA-8200 Superprobe, JEOL Ltd.) were also employed, operated at an accelerating voltage of 15 kV, a beam current of 20 nA, and a beam size of 1 μm.

Chemical analysis of flotation and magnetic separation products were analyzed via inductively coupled plasma optical emission spectroscopy (ICP-OES), leached in hydrofluoric acid.

Thermodynamic Analysis

Thermodynamic analysis was conducted with FactSage 8.0 using the FactPS and FToxid databases supplemented with literature data[51–60]. Calculated gas volumes as a function of temperature are included in Table S31. Critical sulfur and oxygen partial pressures for metal reduction were calculated using the Reaction module. Sulfidation gas ratios and diagrams were calculated using the Predom module, with critical gas ratios for sulfidation found by taking the intersection of phase domains with the relevant pressure isobars[61]. Equilibrium interactions between S-O gasses and carbon were calculated using the Equilib module, with CS_2 formation taken to be suppressed[62], and are included in Table S32. Detailed thermodynamic methodologies are included in the supplemental materials.

Kinetics of Lanthanum Oxide Sulfidation

The following reactions were taken to describe the net sulfidation of lanthanum oxide and gaseous diatomic sulfur with inclusion of a carbon source. While other gas reactions were also present, the species involved were found to be dilute and their role in the sulfidation kinetics was therefore ignored.

$$La_2O_3 + \frac{25}{12}S_2 = \frac{2}{3}La_3S_4 + \frac{3}{2}SO_2 \qquad (1)$$

$$\frac{2}{3}La_3S_4 + \frac{1}{6}S_2 = La_2S_3 \qquad (2)$$

$$SO_2 + 2C = 2CO + \frac{1}{2}S_2 \qquad (3)$$

La_3S_4 is a “lower” sulfide product that occurs prior to the formation of La_2S_3, in addition to the formation of an intermediate oxysulfide, La_2O_2S. With this proposed mechanism, the reaction of La_3S_4 to La_2S_3 is indiscernible in IR product gas analysis (see above) due to the fact that no additional oxygen-containing gasses would be liberated during the sulfidation of La_3S_4 to La_2S_3, while the reactions of La_2O_3 to La_2O_2S and La_2O_2S to La_3S_4 are indistinguishable in the gas signal due to their simultaneous occurrence within the packed bed reactor. Carbothermic refluxing of SO_2 to S_2 (Eq. 3) is taken to be fast compared to sulfidation. The sulfidation reaction is taken to be zero order with regard to concentration of the solid, and the gasses are assumed to form an ideal gas mixture, resulting in a rate law of the following form on a per unit volume basis, where $r_{La_3S_4}$ is the rate of formation of La_3S_4, r_{SO_2} is the rate of formation of SO_2, r_{CO} is the rate of formation of CO, r_O is the corresponding rate of oxygen liberation during sulfidation, k is the observed reaction rate constant, n is the reaction order in S_2, P_{S_2} is the S_2 partial pressure, R is the gas constant, and T is the absolute temperature:

$$r_{La_3S_4} = \frac{4}{9}r_{SO_2} + \frac{8}{9}r_{CO} = \frac{18}{25}k\left(\frac{P_{S_2}}{RT}\right)^n [=] \left(\frac{mol_{La_3S_4}}{m^3}\right)s^{-1} \qquad (4)$$

$$r_O = \frac{9}{2}r_{La_3S_4} = \frac{81}{25}k\left(\frac{P_{S_2}}{RT}\right)^n [=] \left(\frac{mol_O}{m^3}\right)s^{-1} \qquad (5)$$

$$k [=] \left(\frac{m^3}{mol}\right)^{n-1} s^{-1} \tag{6}$$

Considering the density of the rare earth oxide, the reaction rate (r') can also be described on an oxide mass basis with the following form, where ρ_B is the bulk density of the solid pellet, $\rho_{La_2O_3}$ is the density of the oxide, and ϵ is the porosity of the pellet:

$$r'_{La_3S_4} = \frac{4}{9} r'_{SO_2} + \frac{8}{9} r'_{CO} = \frac{18}{25} \frac{k}{\rho_B} \left(\frac{P_{S_2}}{RT}\right)^n [=] \left(\frac{mol_{La_3S_4}}{kg_{La_2O_3}}\right) s^{-1} \tag{7}$$

$$r'_O = \frac{9}{2} r'_{La_3S_4} = \frac{81}{25} \frac{k}{\rho_B} \left(\frac{P_{S_2}}{RT}\right)^n [=] \left(\frac{mol_O}{kg_{La_2O_3}}\right) s^{-1} \tag{8}$$

$$k' = \frac{k}{\rho_B} [=] \left(\frac{m^3}{mol}\right)^{n-1} \frac{m^3}{kg} s^{-1} \tag{9}$$

$$\rho_B = \rho_{La_2O_3}(1-\epsilon) \tag{10}$$

Considering surface area of the rare earth oxide, the reaction can be described on an oxide surface area basis with the following form, where S is the specific surface area:

$$r''_{La_3S_4} = \frac{4}{9} r''_{SO_2} + \frac{8}{9} r''_{CO} = \frac{18}{25} \frac{k}{\rho_B S} \left(\frac{P_{S_2}}{RT}\right)^n [=] \left(\frac{mol_{La_3S_4}}{m^2{}_{La_2O_3}}\right) s^{-1} \tag{11}$$

$$r''_O = \frac{9}{2} r''_{La_3S_4} = \frac{81}{25} \frac{k}{\rho_B S} \left(\frac{P_{S_2}}{RT}\right)^n [=] \left(\frac{mol_O}{m^2{}_{La_2O_3}}\right) s^{-1} \tag{12}$$

$$k'' = \frac{k}{S_{Ln_2O_3} \rho_B} [=] \left(\frac{m^3}{mol}\right)^{n-1} \frac{m}{s} \tag{13}$$

In general, the initial rate of reaction and partial pressures are typically utilized to determine reaction kinetics. The observed reaction order and rate constant can be found by fitting IR gas signal data for sulfur and oxygen containing species to the following relation, where $m_{La_2O_3}$ is the initial mass of oxide:

$$\ln r'_O = n \ln\left(\frac{P_{S_2}}{RT}\right) + \ln\left(\frac{81}{25} \frac{k m_{La_2O_3}}{\rho_{Ln_2O_3}(1-\epsilon)}\right) \tag{14}$$

The observed activation energy ($-E_A$) and Arrhenius pre-exponential factor (A_r) are found by fitting the natural log of k versus T^{-1} to the natural log of the Arrhenius equation:

$$\ln k = \frac{-E_A}{RT} + \ln A_r \quad (15)$$

However, for a fluid-solid reaction, the observed initial rate of reaction does not inherently reflect the intrinsic chemical rate due to the presence of internal (within the porous solid) and external (to the surface of the porous solid) mass transfer limitations[25,63,64]. In order the measure intrinsic chemical kinetics, experiments must be performed in regimes where both internal and external mass transfer limitations are shown to be negligible. Intrinsic chemical kinetics are distinguished from external, intergrain, and intragrain mass transfer limitations following the methodologies of Sohn et al[25,64–68] and relevant literature data[69–73], detailed in the Supplemental Materials.

Derivation of Critical Gas Flowrates for Sulfidation

The role of solid carbon on the carbothermically-driven sulfur reflux (CDSR) of SO_2 back into S_2 (Eq. 3) is modelled to determine the P_{S2}/P_{SO2} ratio in the active volume of the reactor. Steady state reactor conditions, a well-mixed gas phase, and a fixed reactor bed were assumed. Carbon-disulfide (CS_2) formation from the reaction of sulfur with elemental carbon is taken to be kinetically-suppressed[62], with other C-S-O reactions taken to be fast compared to the sulfidation reaction, existing at quasi-equilibrium, tabulated in Table S32. For different carbon sources or reactors with different transport phenomena, CS_2 formation may be present, yet may still be accounted for by following the framework herein. Mass transfer limitations, including the effects of sintering, can be captured by scaling the sulfidation reaction rate constant by a kinetic effectiveness factor, derived following the methodology of the Theile modulus in heterogeneous catalysis[63]. By conducting a mass balance over the rate of gas introduction into the reactor, the rate of the sulfidation reaction, the rate of CDSR, and the rate of gas phase reactions with SO_2, the maximum average gas residence time to support sulfidation, known as the space time (τ_{space}^{max}), and its inverse known as the minimum space velocity (v_{space}^{min}), may be calculated as a function of sulfidation kinetics, reaction temperature, carbon feed content, and $[P_{S2}/P_{SO2}]_{crit}$. Derivation of τ_{space}^{max} and v_{space}^{min} are detailed in the supplemental materials.

Technoeconomic Study

The capital cost (CAPEX) of a generic, binary metal separation from equimolar mixed oxides is estimated for hydrometallurgical processing, consisting of acid roasting for impurity removal and formation of soluble metal compounds, product gas treatment, leaching of the target elements, solvent extraction for metal element separation, and precipitation of product metal compounds. Mixer-settler and pulsed column liquid-liquid separators are sized based on process chemistry and conditions[48,74–77], each operating at hydrometallurgical separation factors of 1.5 and 10,000, representative of f-block and d-block element separations respectively[8,75,77]. Meanwhile, the CAPEX of the same separation via selective sulfidation is estimated by considering air separation for nitrogen carrier gas production, sulfidation in a multihearth fluidized bed reactor, comminution, physical separation via froth flotation, and waste gas stream handling via a cyclone separator, followed by either electrostatic solids precipitator and dual alkali scrubbing (when the carbothermically-driven sulfur reflux, CDSR, is utilized in sulfidation) or sulfuric acid production (No CDSR). Materials containing impurities such as normally occurring radioactive elements or anions other than oxygen and sulfur may require additional pretreatments prior to selective sulfidation. The CAPEX of some possible material feed preparation steps are also considered, such as feed drying, calcination for defluorination of fluorocarbonate minerals or lithium ion battery electrolytes and oxidation of mixed metal compounds such as rare earth magnets, sulfidation for dephosphorization of phosphate minerals and dethoriation of rare earth concentrates, and sulfidation/calcination for sintering of material feeds too finely ground for effective liberation and physical separation of sulfide precipitants post selective sulfidation. The CAPEX of individual unit operations is estimated using scaling relations based on equipment size, energy usage, throughput, or other relevant operating parameters[48,78,79], which are included in Table S14 and discussed in the Supplemental Materials. Location factors[76] (Table S33) may be employed to consider geographic differences. For all CAPEX cost curves utilized herein, American Association of Cost Engineers International Class 4 methodology is employed, with an error of ±30%[80].

Operating costs (OPEX) of the generic selective sulfidation processes described above are estimated from reagent, utility, and waste treatment usage and prices, correlations for labor costs with relevant chemical process unit operations, correlations for management and overheads with labor cost, and correlations for maintenance costs with CAPEX[76,78,79,81–88]. Revenue credits from byproduct sulfuric acid production are excluded in OPEX analysis. OPEX as estimated herein does not include processing steps upstream of selective sulfidation and its supporting pretreatments, such as mining and preliminary comminution / mineral dressing in primary production from ores, or material collection and crushing / disassembly in secondary materials production from recycled materials. These upstream steps are not considered since they are necessary regardless of the downstream materials separation technique employed (leaching, solvent extraction, pyrometallurgical smelting, selective sulfidation, etc.), and may or may not be conducted at the same facility as downstream materials processing. Likewise, differences in costs between established and greenfield facilities are not considered herein.

Sensitivity analysis for OPEX and CAPEX is conducted via Monte Carlo simulation[76] at selective sulfidation feed capacities of 10, 100, and 1000 kilotonnes per year. At each feed capacity, 360,000 iterations of the CAPEX and OPEX models were conducted. Operating parameters, reagent costs, labor requirements and costs, yearly maintenance cost as a fraction of CAPEX, Class 4 CAPEX error (+/-30%), and geographic scaling factors were each randomly varied using continuous triangular distributions centered around known or calculated values, as outlined in Tables S15 and S17. When uninformed by literature, upper and lower bounds for triangular distributions were taken as -50 to +100% of the base value[76]. Thermodynamic inputs for mass and energy balances were randomly varied using coupled discrete, uniform distributions across the sulfidation chemistries of copper (Cu_2O), neodymium, and nickel oxides (NiO) each with and without employment of CDSR, as outlined in Table S16.

For technoeconomic assessment of selective sulfidation, mass balances, energy balances, and economic data are calculated using spreadsheets constructed in Microsoft Excel. Bounds for variables are tabulated in separate Excel spreadsheets (Table S16-S17), with variable distributions used in Monte Carlo sensitivity analysis generated and iteratively substituted into the spreadsheets for mass balances, energy balances, and economic data using MATLAB scripts. CAPEX and OPEX results are iteratively read and aggregated using separate MATLAB scripts.

For technoeconomic assessment of hydrometallurgical processes, economic data calculations and Monte Carlo sensitivity analysis are conducted using MATLAB scripts, with variable bounds tabulated in an Excel spreadsheet (Table S15). The implementation and integration of MATLAB scripts with Excel are further discussed in the supplemental materials. MATLAB scripts and Excel spreadsheets are available as described in Code Availability.

Environmental Impact Study

The environmental impact of selective sulfidation is estimated for the same generic materials separation processes considered in the Technoeconomic Study via life cycle assessment (LCA) across the impact categories of global warming potential (GWP), terrestrial acidification (TA), and water resource depletion (WRD). The system boundary is defined to be an input of mixed-metal oxide and an output of physically-separated oxide and sulfide. A functional unit of 1 kg of feed oxide is utilized to avoid making assumptions about feed grade or product yield. Processing pathways with and without feed pretreatments (Technoeconomic Study) and with and without carbothermically-driven sulfur reflux (CDSR) are considered, and shown with system boundaries in Figures E8 and S1-S3. To avoid the need for allocation of environmental impacts between coproducts as recommended by ISO 14040[89], system boundaries are established so that the impacts associated with any by-and or coproducts are fully attributed to processing the feed oxide. Life cycle intensity data for inputs into the generic sulfidation process are derived from ecoinvent 3.6[90] global averages and representative literature data[91–93], with impacts quantified using TRACI 2.1[94] and other United States Environmental Protection Agency and Unite States Energy Information Agency data[95]. Sensitivity analyses is conducted using Monte Carlo simulation as outlined in the Technoeconomic Study and discussed in the Supplemental Materials.

Due to the strong dependence of environmental impact on system chemistry observed in the Monte Carlo simulation, the environmental impacts of utilizing selective-sulfidation-based pathways are calculated for three case studies via LCA. Zirconium-silicon separation from zircon, iron-titanium separation from ilmenite, and rare earth element separation from bastnaesite are considered. These case studies are selected for two reasons: 1 – the existing processes – alkali fusion, the sulfate process, and acid roasting/leaching/solvent extraction respectively –

each involve a combination of non-selective pyrometallurgical and selective hydrometallurgical processes, serving to elucidate the possible environmental impact reduction by increasing the selectivity of pyrometallurgical treatments using sulfidation chemistry. 2 – each of these processes has well-documented feed chemistry, LCA data, system boundaries, and allocation strategies for the standard processing route[9,49], supporting fair comparison of impacts between selective sulfidation with physical separation and hydrometallurgical chemical separation.

The environmental impact of zirconium oxide and silicon oxide separation from zircon is compared between the standard alkali fusion process and selective sulfidation using LCA. Environmental impact data for alkali fusion is available in a published study[49]. System boundaries for selective sulfidation are defined to be an input of zircon, and an output of silicon and mixed zirconium-hafnium oxide as shown in Figure S7. Processing steps and assumptions are detailed in Supplemental Materials. A functional unit of 1 kg of zirconium oxide is adopted for the impact categories of GWP, TA, and WRD. Division of environmental impacts between coproducts is conducted via the ISO 14040[89] hierarchy. Allocation of impacts between zirconium and hafnium product oxides are conducted on a mass basis, as described in Table S25. The same allocation fractions are adopted herein as those for the published study[49] on the alkali fusion process, supporting equitable comparison of impacts between the pathways. The detailed life cycle inventory (LCI) for selective sulfidation is included in Table S22 and discussed in the Supplemental Materials. Supporting sulfidation thermodynamic data is derived from FactSage 8.0 and is included in Table S29.

The environmental impact of iron-titanium oxide separation from ilmenite is compared between the standard sulfate process and selective sulfidation using life cycle assessment. LCA impact data for the sulfate process is available in a published study[49]. System boundaries for selective sulfidation are defined to be an input of ilmenite, and an output of titanium dioxide and iron sulfide, as shown in Figure S8. Processing steps and assumptions are detailed in Supplemental Materials. A functional unit of 1 kg of titanium dioxide is adopted for the impact categories of GWP, TA, and WRD. As for the published[49] LCA of the sulfate process, environmental impacts for processing of ilmenite to titanium dioxide are fully attributed to titanium dioxide production, supporting equitable comparison of impacts between the two pathways and eliminating the need for environmental impact allocation. The detailed LCI for selective sulfidation is included in Table S23 and discussed in the Supplemental Materials. Supporting sulfidation thermodynamic data is derived from FactSage 8.0 and is included in Table S30.

The environmental impact of rare earth element separation from bastnaesite, the most commercially-relevant source of light rare earth elements, is compared between the standard acid roasting, leaching, and solvent extraction pathway and selective sulfidation using LCA. Environmental impact data for the standard hydrometallurgical route is available in a published study[9]. System boundaries for selective sulfidation are defined to be an input of pre-concentrated (non-defluorinated, non-dethoriated) bastnaesite rare earth fluorocarbonate, and an output of separated rare earth element compounds as shown in Figures S9-S10, processed at the world's largest rare earth element producer at the Bayan Obo facility in China, with processing steps and assumptions detailed in the Supplemental Materials. A functional unit of 1 kg of separated rare earth elements is adopted for the impact categories of GWP, TA, and WRD. To avoid the need for allocation of environmental impacts between coproducts as recommended by ISO 14040[89], environmental impacts are reported on the basis of total mass of separated rare earth oxide. This eliminates the need for allocation of environmental impact between rare earth oxide by- and coproducts, and supports fair comparison of environmental impacts to the published study[9] on the hydrometallurgical route, which also reports impacts for a functional unit of 1 kg of total separated rare earth oxides. The detailed LCI for selective sulfidation is included in Table S24 and discussed in the Supplemental Materials. Supporting sulfidation thermodynamic data is derived from FactSage 8.0, using neodymium (III) oxide as a model system, and is included in Table S28.

For environmental assessment of selective sulfidation, mass and energy balances are calculated using the same spreadsheets as for technoeconomic evaluation. Bounds for variables are tabulated in separate Excel spreadsheets (Table S16-S17), with variable distributions used in Monte Carlo sensitivity analysis generated and iteratively substituted into the spreadsheets for mass balances, energy balances, and economic data using MATLAB scripts. Mass and energy balance results are iteratively read and aggregated using separate MATLAB scripts, where they are converted to environmental impacts. The implementation and integration of MATLAB scripts with Excel are further discussed in the supplemental materials[96]. MATLAB scripts and Excel spreadsheets are available as described in Code Availability.

Methods References

51. Jacob, K. T. & Iyengar, G. N. K. Thermodynamic study of Fe2O3-Fe2(SO4)3 equilibrium using an oxyanionic electrolyte (Na2SO4-I). *Metall. Trans. B* **17**, 323–329 (1986).

52. Hsieh, K. C. & Chang, Y. A. A solid-state emf study of ternary Ni-S-O, Fe-S-O, and quaternary Fe-Ni-S-O. *Metall. Trans. B* **17**, 133–146 (1986).

53. Dwivedi, R. K. & Kay, D. A. R. Thermodynamics of the oxidation of rare earth oxysulfides at high temperatures. *Metall. Trans. B* **15**, 523–528 (1984).

54. Akila, R., Jacob, K. T. & Shukla, A. K. Gibbs Energies of Formation of Rare Earth Oxysulfides. *Metall. Trans. B* **18B**, 163–168 (1987).

55. Dwivedi, R. K. Determination of the Thermodynamic Properties of Rare Earth-Oxygen-Sulfur Systems at High Temperatures. *PhD Thesis* (McMaster University, 1982).
56. Suponitskii, Y. L., Kuz'micheva, G. M. & Eliseev, A. A. Lanthanide Oxide Sulphides. *Russ. Chem. Rev.* **57**, 209–220 (1988).
57. Wang, M. Enthalpy of formation of LiNiO2, LiCoO2 and their solid solution, LiNi1−xCoxO2. *Solid State Ionics* **166**, 167–173 (2004).
58. Chang, K., Hallstedt, B. & Music, D. Thermodynamic and Electrochemical Properties of the Li−Co−O and Li−Ni−O Systems. *Chem. Mater.* **24**, 97–105 (2011).
59. Konings, R. J. M. *et al.* The Thermodynamic Properties of the f-Elements and their Compounds . Part 2 . The Lanthanide and Actinide Oxides The Thermodynamic Properties of the f -Elements and their Compounds . Part 2 . The Lanthanide and Actinide Oxides. *J. Phys. Chem. Ref. Data* **43**, 013101 (2014).
60. Kriklya, A. I., Bolgar, A. S. & Pribyl'skii, N. Y. Heat Capacity and Enthalpy of y-Dy2S3 Over a Wide Range of Temperature. *Sov. Powder Metall. Met. Ceram.* **31**, 697–700 (1992).
61. Chakraborti, N. Modified predominance area diagrams for the Fe- S- O system. *Can. J. Chem. Eng.* **61**, 763–765 (1983).
62. Madon, N. & Strickland-constable, R. F. Production of Carbon Disulfide. *Ind. Eng. Chem.* **50**, 1189–1192 (1958).
63. Fogler, H. S. *Elements of Chemical Reaction Engineering*. (Prentice Hall, 2016).
64. Sohn, H. Y. Review of fluid-solid reaction analysis—Part 2: Single porous reactant solid. *Can. J. Chem. Eng.* **97**, 2068–2076 (2019).
65. Sohn, H. Y. & Szekely, J. A structural model for gas-solid reactions with a moving

boundary—III. *Chem. Eng. Sci.* **27**, 763–778 (1972).

66. Sohn, H. Y. & Szekely, J. The effect of intragrain diffusion on the reaction between a porous solid and a gas. *Chem. Eng. Sci.* **29**, 630–634 (1974).

67. Ishida, M. & Wen, C. Y. Comparison of kinetic and diffusional models for solid- gas reactions. *AIChE J.* **14**, 311–317 (1968).

68. Sohn, H. Y. & Perez-Fontes, S. E. Application of the Law of Additive Reaction Times to Fluid-Solid Reactions in Porous Pellets with Changing Effective Diffusivity. *Met. Mater. Trans. B* **41B**, 1261–1267 (2010).

69. Hirschfelder, J. O., Curtiss, C. F. & Bird, R. B. *Molecular Theory of Gases and Liquids*. (John Wiley & Sons Inc., 1954).

70. Berard, M. F., Wirkus, C. D. & Wilder, D. R. Diffusion of Oxygen in Selected Monocrystalline Rare Earth Oxides. *J. Am. Ceram. Soc.* **51**, 643–647 (1968).

71. Cussler, E. L. *Diffusion: Mass Transfer in Fluid Systems*. (Cambridge University Press, 2009).

72. Deen, W. M. *Introduction to Chemical Engineering Fluid Dynamics*. (Cambridge University Press, 2016).

73. Brown, A. M. & Ashby, M. F. Correlations for Diffusion Constants. *Acta Metall.* **28**, 1085–1101 (1980).

74. Liao, B. Q., Wan, C. R. & Wang, J. A Concept for the Estimation of HETS for Rare Earth Separations in Extraction Columns. *Sep. Sci. Technol.* **39**, 2597–2607 (2004).

75. Flett, D. S. Solvent extraction in hydrometallurgy: the role of organophosphorus extractants. *J. Organomet. Chem.* **690**, 2426–2438 (2005).

76. Towler, G. & Sinnott, R. *Chemical Engineering Design*. (Elsevier, 2013).

77. Cheng, C. Y. & Zhu, Z. Solvent extraction technology for the separation and purification of niobium and tantalum: A review. *Hydrometallurgy* **107**, 1–12 (2011).

78. Dincer, I. & Bicer, Y. *Mitacs Accelerate Project Final Report*. (2015).

79. Green, D. W. & Perry, R. H. *Perry's Chemical Engineer's Handbook*. (McGraw-Hill, 2008).

80. Christensen, P. & Dysert, L. *Cost Estimate Classification System as Applied in Engineering, Procurement, and Construction for the Process Industries*. *AACE International Recommended Practice No. 18R-97 COST, TCM Framework: 7.3 - Cost Estimating and Budgeting* (2005).

81. USGS. *Mineral Commodity Summaries 2021*. (2021).

82. USEIA & USDOE. *Annual Coal Report 2020*. (2021).

83. USEIA. *Henry Hub Natural Gas Spot Price*. (2021).

84. Misaka, T. & Mochizuki, Y. Recent Application and Running Cost of Moving Electrode type Electrostatic Precipitator. *Electrost. Precip.* 518–522 (2009). doi:10.1007/978-3-540-89251-9_103

85. Bleiwas, D. I. *Estimated Water Requirements for the Conventional Flotation of Copper Ores*. *USGS Open-File Report 2012-1089* (2012).

86. Bleiwas, D. I. *Estimates of Electricity Requirements for the Recovery of Mineral Commodities , with Examples Applied to Sub-Saharan Africa*. *USGS Open-File Report 2011-1253* (2011).

87. Bezuidenhout, G. A., Davis, J., van Beek, B. & Eksteen, J. J. Operation of a concentrated mode dual-alkali scrubber plant at the Lonmin smelter. *J. South. African Inst. Min. Metall.* **112**, 657–665 (2012).

88. King, M. J., Davenport, W. G. & Moats, M. S. *Sulfuric Acid Manufacture - Analysis, Control and Optimization*. (2013).

89. ISO. *ISO 14044*. (2006).

90. Ecoinvent-Association. ecoinvent 3.6. *Ecoinvent Center* (2019). Available at: www.ecoinvent.org.

91. Klett, C., Reeb, B., Missalla, M. & Schmidt, H.-W. Methods to Reduce Operating Costs in Circulating Fluidized Bed Calcination. in *Light Metals 2011* 125–130 (John Wiley & Sons, Inc., 2011). doi:10.1002/9781118061992.ch22

92. Fu, C. & Gundersen, T. Using exergy analysis to reduce power consumption in air separation units for oxy-combustion processes. *Energy* **44**, 60–68 (2012).

93. de Bakker, J. Energy Use of Fine Grinding in Mineral Processing. *Metall. Mater. Trans. E* **1**, 8–19 (2014).

94. USEPA. TRACI 2.1. *Tool for Reduction and Assessment of Chemicals and Other Environmental Impacts* (2014). Available at: https://www.epa.gov/chemical-research/tool-reduction-and-assessment-chemicals-and-other-environmental-impacts-traci.

95. USEIA. *Carbon Dioxide Emissions Coefficients*. (2021).

96. Stinn, C., Allanore, A. *Selective Sulfidation of Metal Compounds - Supporting Computing Files*. Harvard Dataverse Repository, Allanore Resaerch Group. (2021). https://doi.org/10.7910/DVN/193PW2

Data Availability

All data relevant to the results presented are included herein, within the supplementary materials, or available from the authors upon request.

Code Availability

Spreadsheets and code supporting technoeconomic analysis and life cycle assessment are available on the Harvard Dataverse Repository, https://doi.org/10.7910/DVN/193PW2.

Acknowledgements

The authors wish to thank the US Department of Energy and the US National Science Foundation for their financial support, H. Higuchi and Sumitomo Metal Mining for providing samples of scandium oxide, and K. Daehn, A. Culbertson, T. Close, L. Rush, A. Caldwell, and M. B. Wagner for their insight.

Author Contributions

C.S. and A.A. designed the project, wrote the manuscript, and prepared the figures. C.S. carried out the experiments, modelling, and analysis.

Competing Interests Declaration

The authors have filed for intellectual property protection pertaining to work herein.

Additional Information

Supplementary information is available for this paper. Correspondence and requests for materials should be addressed to allanore@mit.edu.

Extended Figures

Figure E1: Gas species partial pressures as thermodynamic levers to control compound stability.

a- Sc-O-S Kellogg diagram (T = 1000°C, 1 atm), illustrating the role of P_{S2}, P_{O2}, and P_{SO2} on scandium compound stability. **b-** Fe-O-S-C predominance diagram, illustrating the role of P_{CO}, P_{CO2}, P_{S2}, and P_{SO2} on iron compound stability (P_{S2} fixed at 0.05 atm). The sulfide becomes the only stable compound of Fe in the presence of carbon at increasing P_{S2} values, as for many critical metals including Co, In, Mn, Ni, Sn, W, and Zn. In **a** and **b**, solid lines correspond to phase domains, dotted line correspond to equilibrium gas compositions at 1 atm total pressure, and dashed lines correspond to P_{SO2}.

Figure E2: Reaction and solution contributions to sulfidation selectivity. a,b – For a generic sulfidation reaction where M is a metal, β, γ, δ, ϵ, ζ, and η are stoichiometric factors, $\Delta_r G°$ is the standard Gibbs energy of reaction, a is the activity, P is the partial pressure, R is the gas constant, and T is the absolute temperature, contributions to a stoichiometric-dependent critical P_{S_2}/P_{SO_2} ratio (ψ) for sulfidation to occur may be divided between reaction (ψ_{rxn}) and solution (ψ_{sol}) effects:

$$\frac{4\epsilon}{2\beta\eta+\gamma\epsilon-2\delta\epsilon-\beta\zeta} M_\beta O_\gamma S_\delta + S_2 = \frac{4\beta}{2\beta\eta+\gamma\epsilon-2\delta\epsilon-\beta\zeta} M_\epsilon O_\zeta S_\eta + \frac{2(\gamma\epsilon-\beta\zeta)}{2\beta\eta+\gamma\epsilon-2\delta\epsilon-\beta\zeta} SO_2$$

$$\log_{10}\left(e^{\frac{\Delta_r G°}{RT}}\right) + \log_{10}\left(\frac{{a_{M_\epsilon O_\zeta S_\eta}}^{\frac{4\beta}{2\beta\eta+\gamma\epsilon-2\delta\epsilon-\beta\zeta}}}{{a_{M_\beta O_\gamma S_\delta}}^{\frac{4\epsilon}{2\beta\eta+\gamma\epsilon-2\delta\epsilon-\beta\zeta}}}\right) = \log_{10}\left(\frac{P_{S_2}}{{P_{SO_2}}^{\frac{2(\gamma\epsilon-\beta\zeta)}{2\beta\eta+\gamma\epsilon-2\delta\epsilon-\beta\zeta}}}\right) = \psi$$

$$\log_{10}\left(e^{\frac{\Delta_r G°}{RT}}\right) = \psi_{rxn}$$

$$\log_{10}\left(\frac{{a_{M_\epsilon O_\zeta S_\eta}}^{\frac{4\beta}{2\beta\eta+\gamma\epsilon-2\delta\epsilon-\beta\zeta}}}{{a_{M_\beta O_\gamma S_\delta}}^{\frac{4\epsilon}{2\beta\eta+\gamma\epsilon-2\delta\epsilon-\beta\zeta}}}\right) = \psi_{sol}$$

When $\psi_{rxn} \gg \psi_{sol}$, the sulfidation thermodynamics are reaction-dominated, solution effects are minimal, and the sulfidation thermodynamics are well-described by those of the pure compound. When $\psi_{sol} \gg \psi_{rxn}$, the sulfidation thermodynamics are solution-dominated and reaction effects are minimal, the sulfidation thermodynamics are not well-described by those of the pure compound, and knowledge of the solution behavior is essential to determine sulfidation spontaneity. **c,d** - Equilibrium sulfur to sulfur dioxide ratio as a function of sulfur partial pressure and temperature at 1 atm for a gas consisting exclusively of sulfur-oxygen-containing species at equilibrium. As derived in the Supplemental Materials, the equilibrium P_{S_2} / P_{SO_2} ratio that satisfies ψ corresponds to $\left[\frac{P_{S_2}}{P_{SO_2}}\right]_{crit}$.

Figure E3: Packed-bed flow-through reactor employed for selective sulfidation (a) and Hallimond cell used for flotation separation of sulfides from oxides (b).

Figure E4: Lanthanum oxide sulfidation reaction kinetics as measured in a graphite packed bed reactor. a – Conversion vs time as a function of temperature shows reaction rate increasing with temperature, consistent with the notion of thermal activation of the reaction. **b** – Sulfur partial pressure corresponding to conversion rate in **a**. **c** – Modified Sherwood number (Sh') for lanthanum oxide sulfidation kinetics experiments. Following Sohn's criteria[65], for $Sh' > 30$ external mass transfer limitations to the observed reaction rate are negligible. **d.** – Fluid-solid reaction modulus ($\hat{\sigma}$) for lanthanum oxide sulfidation kinetic experiments. For $\hat{\sigma}^2 < 0.01$, intergrain diffusion limitations to the observed rate of reaction are negligible[65]. Intragrain diffusion limitations are addressed in the Supplemental Materials and Table S3. **e** – Comparison of the kinetically-limited (Supplemental Materials) rate of oxygen liberation for sulfidation vs sulfur gas concentration. The slope of natural log of the oxygen liberation rate vs the natural log of the sulfur concentration is the reaction order, observed to be approximately first order with respect to sulfur. **f** – Arrhenius plot of the natural log of the reaction rate constant vs inverse temperature. The activation energy is found to be 114 kJ/mol, with a pre-exponential factor of 1.08×10^4 s^{-1}.

Figure E5: Selective sulfidation of $LiNi_{1/3}Mn_{1/3}Co_{1/3}O_2$ (abbr. NMC111 or NMC333) separated into Ni-rich sulfide (1), Co-rich sulfide (2), and Mn oxysulfide (3) phases. a- Optical dark field image showing Ni, Co, and Mn-rich phases coalesced to approximately 100-500 µm in size that support physical separation following at 1000°C. **b-** SEM-EDS analysis reveals distinct Ni-rich sulfide (1, $Ni_{0.75}Co_{0.25}S$), Co-rich sulfide (2, $Ni_{0.33}Co_{0.67}S$), and Mn oxysulfide (3, $MnO_{0.2}S_{0.8}$) phases. **c-** SEM-EDS maps illustrate minimal Mn inclusion in Ni-Co phases and vice versa post-sulfidation.

Figure E6: Selective sulfidation of calcined rare earth, iron, boron ((Nd,Pr,Dy)-Fe-B) magnet separated into an iron-rich sulfide phase (1) with neodymium-rich oxide (2) inclusions. a – Upon sulfidation, calcined (Nd,Pr,Dy)-Fe-B particles 90-212 μm in size sintered to approximately 1-2 mm in size, with Nd-rich oxide (1) regions approximately 20-100 μm in size that are large enough to support physical separation from the bulk Fe-rich sulfide (2) phases (SEM/BEC image). **b** – SEM-EDS analysis reveals minimal inclusion of Fe,Dy into the Nd,Pr-rich inclusions and vice versa post-sulfidation.

Figure E7: Sulfidative sintering and selective sulfidation of synthetic defluorinated, dethoriated, light rare earth element bastnaesite (Ln_2O_3) separates into neodymium-rich and lanthanum-rich phases. a – Ln_2O_3 particles (25-45 μm) sulfidized with carbon in an alumina flow-through packed-bed reactor at 1400°C sintered to approximately 100-300 μm in size (darkfield optical image). **b** – $Ln_{10}OS_{14}$ (1) and Ln_2O_2S (2) approximately 20-100 μm in size are observed to form upon sulfidation, large enough to support physical separation (polarized optical image, 90°). **c** – EPMA/WDS elemental analysis reveals sulfidation is selective, with Nd enriched in the oxygen-rich Ln_2O_2S phase (2) and La enriched in the sulfur-rich $Ln_{10}OS_{14}$ phase (1).

Figure E8: Flowsheet of a generic selective sulfidation process. The process consists of selective sulfidation in a multihearth fluidized bed reactor, product comminution and physical separation via froth flotation, and downstream gas handling and treatment via a cyclone separator for solid particle removal and acid plant for SO_2 recovery, and assumes an equimolar, mixed, binary oxide feed. The system boundary for life cycle assessment is depicted, over the impact categories of global warming potential (GWP), terrestrial acidification (TA), and water resource depletion (WRD), for a functional unit of 1kg of selective sulfidation feed. The impacts of flows originating within the system boundary are evaluated from the cradle to usage in the process, while the impacts of flows originating outside the system boundary are evaluated from the system gate to usage in the process. The impacts of flows exiting within the system boundary are evaluated from outlet of the process to the grave, while flows exiting outside the system boundary are evaluated from production in the process to the system gate.

Figure E9: Capital cost (CAPEX) and operating cost (OPEX) distributions for the generic selective sulfidation process (Figures E8, S1-S3). Distributions for selective sulfidation with and without feed pretreatments and with and without carbothermically-driven sulfur reflux (CDSR) are determined via Monte Carlo simulation, with probability distribution for CAPEX, OPEX, and operating condition parameters described in Tables S14-S15. Pretreatment steps for feed drying, sintering, and roasting/calcination each marginally increase the CAPEX and OPEX of selective sulfidation by 10% to 20%. CDSR generally decreases CAPEX at the expense of increases in OPEX and environmental impacts (Figure E10).

Figure E10: Global warming potential (GWP), water resource depletion (WRD), and terrestrial acidification (TA) distributions for the generic selective sulfidation process (Figures E8, S1-S3), with and without feed pretreatments, with and without carbothermically-driven sulfur reflux (CDSR), for a functional unit of 1 kg of selective sulfidation feed. Distributions are determined via Monte Carlo simulation, with probability distribution for operating condition parameters described in Tables S14-S15. The inclusion of feed pretreatments increases GWP by about 50%, WRD by 30% and TA by double, while CDSR increases GWP by a factor of 3-5x and WRD by a factor of 3-4x. The bimodal nature of the GWP distribution is due to differences in oxygen content of the three model chemistries considered in the Monte Carlo simulation, highlighting the role of system chemistry in determining environmental impact.

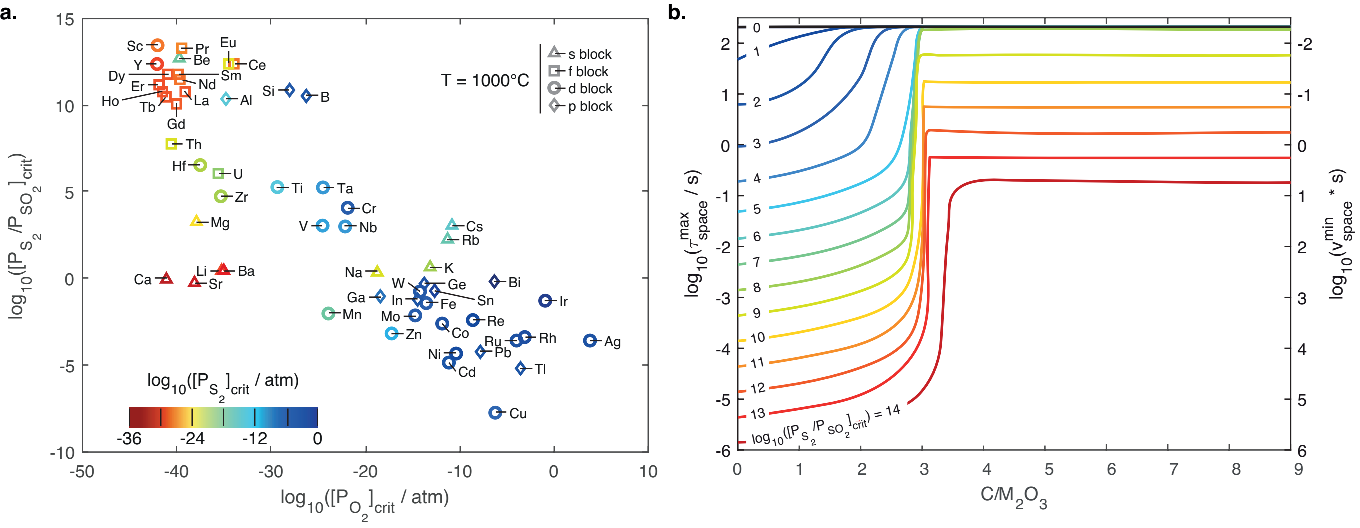
a.
T = 1000°C
s block
f block
d block
p block
Sc
Pr
Eu
Y
Be
Ce
Dy
Sm
Er
Nd
Ho
La
Tb
Gd
Al
Si
B
Th
Hf
U
Zr
Ti
Ta
Cr
Mg
V
Nb
Cs
Rb
Ca
Li
Ba
Sr
Na
K
W
Ge
Bi
Ga
In
Fe
Sn
Ir
Mn
Mo
Re
Zn
Co
Ru
Rh
Ag
Ni
Pb
Cd
Tl
Cu
$\log_{10}([P_{S_2}]_{crit}$ / atm)
-36
-24
-12
0
15
10
5
0
-5
-10
-50
-40
-30
-20
-10
0
10
$\log_{10}([P_{O_2}]_{crit}$ / atm)
$\log_{10}([P_{S_2}/P_{SO_2}]_{crit})$
b.
0
1
2
3
4
5
6
7
8
9
10
11
12
13
$\log_{10}([P_{S_2}/P_{SO_2}]_{crit}) = 14$
2
1
0
-1
-2
-3
-4
-5
-6
-2
-1
0
1
2
3
4
5
6
0
1
2
3
4
5
6
7
8
9
C/M_2O_3
$\log_{10}(\tau_{space}^{max}$ / s)
$\log_{10}(v_{space}^{min}$ * s)

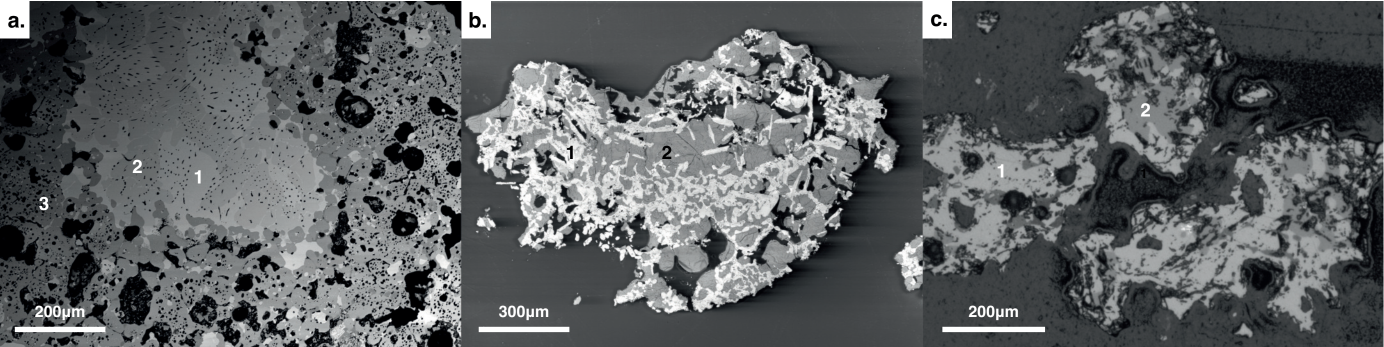
a.
1
2
3
200μm
b.
1
2
300μm
c.
1
2
200μm

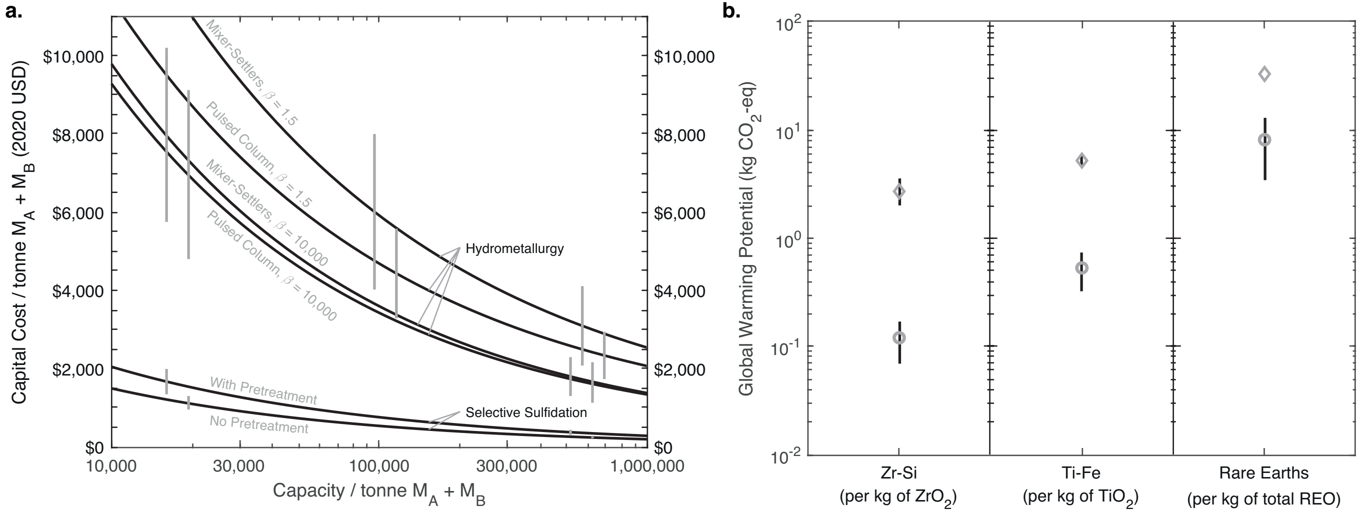
a.
Capital Cost / tonne $M_A + M_B$ (2020 USD)
$10,000
$8,000
$6,000
$4,000
$2,000
$0
Mixer-Settlers, β = 1.5
Pulsed Column, β = 1.5
Mixer-Settlers, β = 10,000
Pulsed Column, β = 10,000
Hydrometallurgy
With Pretreatment
No Pretreatment
Selective Sulfidation
10,000
30,000
100,000
300,000
1,000,000
Capacity / tonne $M_A + M_B$
b.
Global Warming Potential (kg CO_2-eq)
10^2
10^1
10^0
10^{-1}
10^{-2}
Zr-Si (per kg of ZrO_2)
Ti-Fe (per kg of TiO_2)
Rare Earths (per kg of total REO)